J. Fluid Mech. (2011), *vol.* 675, *pp.* 347–368.
doi:10.1017/jfm.2011.21

Granular column collapses down rough, inclined channels

GERT LUBE[1], HERBERT E. HUPPERT[2]†, R. STEPHEN J. SPARKS[3] AND ARMIN FREUNDT[4]

[1]Volcanic Risk Solutions, Massey University, Palmerston North, Private Bag 11222, New Zealand

[2]Department of Applied Mathematics and Theoretical Physics, Institute of Theoretical Geophysics, Centre for Mathematical Sciences, University of Cambridge, Wilberforce Road, Cambridge CB3 0WA, UK

[3]Department of Earth Sciences, Centre of Environmental and Geophysical Flows, Bristol University, Bristol BS8 1RJ, UK

[4]Research Division 'Dynamics of the Ocean Floor,' IFM-GEOMAR, Leibniz Institute for Marine Sciences, Wischhofstrasse 1-3, D-24148 Kiel, Germany

(Received 12 August 2008; revised 23 December 2010; accepted 6 January 2011; first published online 4 April 2011)

We present experimental results for the collapse of rectangular columns of sand down rough, inclined, parallel-walled channels. Results for basal inclination θ varying between 4.2° and 25° are compared with previous results for horizontal channels. Shallow-water theory can be usefully combined with scaling relationships obtained by dimensional analysis to yield analytical functions of the maximum runout distance, the maximum deposit height and the time to reach the maximum runout. While the theory excellently predicts the maximum lengths of the deposit it generally overestimates the runout time. The inertial flows are characterized by a moving internal interface separating upper flowing and lower static regions of material. In an initial free-fall phase of collapse the deposited area (= volume per unit width) below the internal interface varies with the square-root of time, independent of the initial height of the column and channel inclination. In the subsequent, lateral spreading phase the deposition rate decreases with increasing basal inclination or with decreasing initial height. The local deposition rate at any fixed distance is a constant, dependent on the column aspect ratio, the channel inclination and the longitudinal position, but invariant with flow velocity and depth. In the lateral spreading phase, vertical velocity profile in the flowing layer take a universal form and are independent of flow depth and velocity. They can be characterized by a shear rate as a function of channel inclination and a length scale describing the fraction of the column involved in flow.

Key words: granular media

1. Introduction

The physical behaviour of the flow of granular media is a relatively young research discipline under active study at the moment. Its ubiquitous applications in industrial processes, engineering problems and agriculture, and its prominence in geological

† Email address for correspondence: heh1@esc.cam.ac.uk

processes have resulted in interdisciplinary investigations from a wide range of research fields. Of particular interest for the hazard assessment of geophysical mass flows is the flow and deposition behaviour in granular free-surface flows driven by gravity.

Currently, there are two major problems in understanding natural particulate flows, such as avalanches of debris or snow, or pyroclastic flows formed in explosive volcanic eruptions. First, measurements on active flows are sparse. Except for some recent field studies on snow avalanches (Gauer *et al.* 2006), measurements are restricted to approximations of the velocity of the flow front. Most of our current knowledge on flow and deposition mechanisms stems from interpretations of their final deposits, which remain qualitative since the detailed mechanisms of deposition are unknown. The second problem is that, although a number of theories and governing equations for particular aspects of granular flow have been established, these mostly describe flows of mono-disperse particles in steady, uniform motion. Possibly the most-investigated situation of gravitational free-surface flows is the motion of thin frictional sheets of particles at inclinations close to the static angle of repose (AOR) (e.g. Savage & Hutter 1989; Hutter *et al.* 1995; Pouliquen 1999; Pouliquen & Forterre 2002). A review of the models for chute and heap flows, as well as flows in rotating drums, was recently published by Midi (2004). Geophysical mass flows, however, are characterized by their unsteady form of motion at high mobility as they propagate over terrain well below the AOR, and time- and space-dependent processes of erosion and deposition.

Recently, a number of studies initiated the investigation of thick, inertial granular flows formed by the sudden release of vertical columns of particles. So far, investigations have focussed on the flow behaviour above a horizontal base and have considered unhindered axisymmetric collapses from cylinders (Huppert *et al.* 2003; Lajeunesse, Mangeney-Castelnau & Vilotte 2004; Lube *et al.* 2004) and wall-bounded collapses from rectangular columns into channels (Huppert *et al.* 2003; Huppert *et al.* 2004; Balmforth & Kerswell 2005; Kerswell 2005; Lajeunesse, Monnier & Homsy 2005; Lube *et al.* 2005; Mangeney-Castelnau *et al.* 2005; Siavoshi & Kudrolli 2005; Staron & Hinch 2005; Zenit 2005; Larrieu, Staron & Hinch 2006; Doyle *et al.* 2007; Lube *et al.* 2007; Thompson & Huppert 2007). Granular collapse flows are characterized by their unsteady form of motion, large time-dependent changes of the free surface and the creation of final deposits through the continuous upward propagation of an internal interface separating already deposited material from that still moving. As a consequence of the internal interface motion, the flow propagates on a layer of deposited material (for most of its length), and hence the flow behaviour is independent of the roughness of the rigid base. Furthermore, inertial forces largely dominate frictional (or inter particle) forces except for the very last stage of surface avalanching, which alters the overall shape of the deposits relatively insignificantly. Thus, most aspects of flow are also largely independent of the grain type. The shape of the deposits, including their maximum vertical and horizontal extension, and the time to reach the final maximum runout can be described solely in terms of the initial geometry of the granular column and the gravitational constant. Such inertial granular collapse flows share a number of characteristics with natural particulate flows, such as the ability to propagate at slopes below the AOR, deposition processes which are dependent on both space and time and the relatively immaterial effect of inter-particle friction.

This study presents experimental results for granular collapse flows into rough, inclined channels that address the following questions: Which additional processes

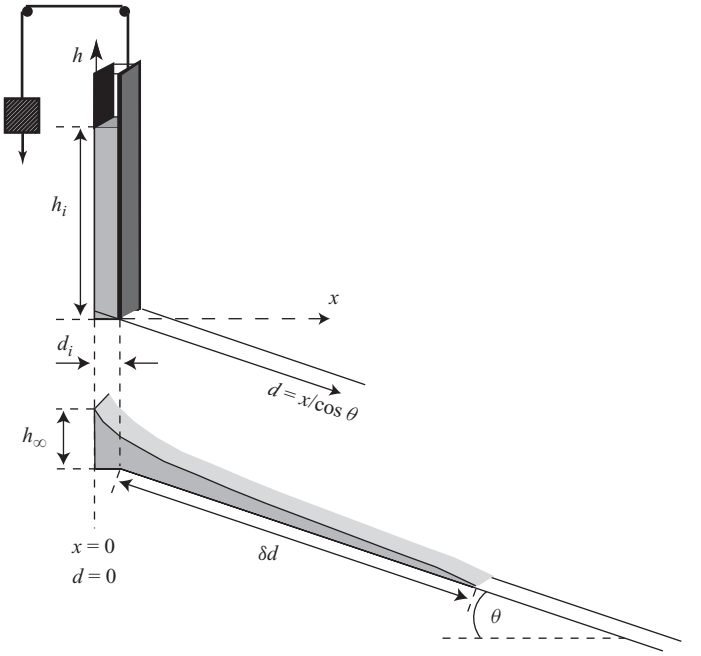

FIGURE 1. The experimental set-up, with a sketch of the initial column of particles (top), the final deposit (bottom) and the definition of the coordinate system used.

occur when the angle of the base of the channel is systematically increased? Up to which inclinations do the mathematical relationships obtained for the horizontal case describe flow behaviour on inclined planes? How does the behaviour of the internal interface and the form of velocity profiles in the flowing layer change with the basal inclination?

The paper is organized as follows. In § 2, we describe the experimental set-up and the measurement techniques. Section 3 briefly summarizes the observed flow behaviour followed by an analysis of the shape of the final deposits in § 4. In § 5, we present an analysis of the temporal aspects of flow as a function of the initial geometry of the column and the basal inclination, with a special focus on the evolution of the internal interface and the vertical velocity profiles in § 6. Finally, in § 7 we summarize and discuss the results obtained.

2. The experiments

2.1. *Experimental set-ups*

The experiments investigate two-dimensional granular flows formed by the collapse of rectangular columns of sand into a 2 m long, inclined channel. The channel had a constant width of 20 cm whose rear panel was constructed of wood and covered with a thin sheet of paper, whereas its frontal panel was of transparent Plexiglas. The basal panel was roughened by gluing sheets of sandpaper with a medium grain size of 0.64 mm to it. The basal inclination of the tank, θ, was varied between 4.2° and 25°. A container accommodated the granular material at one end of the tank (figure 1). A rectangular box of the same width, 20 cm, as the channel and variable initial basal length d_i comprised a frontal gate to release the granular material. A

Basal inclination	Initial basal length d_i (cm)	Range of $a = h_i/d_i$
4.2°	6.3	0.8–14.1
10°	6.3	0.8–7.9
15°	6.05	0.5–14.3
	9.05	3.0–7.0
20°	6.05	3.2–11.7
	9.05	0.2–2.4
25°	6.05	0.4–9.0

TABLE 1. Initial basal length and range of initial aspect ratio for each inclination.

release mechanism was constructed to allow for very fast and reproducible lifting velocities of the gate. The mechanism consisted of releasing a large weight connected to the gate via a pulley construction at the ceiling. The weight fell freely for the first 0.75 m to reach a high velocity (approximately $4\,\mathrm{m\,s^{-1}}$) before it lifted the gate extremely rapidly. The time for the gate release in any experiment was very much less than the typical time scale of the resultant motion of the granular material.

We employed a mixture of rounded, industrial light grey and black coloured Quartz sands of grain size 1.4 ± 0.4 mm with a (static) AOR of $33 \pm 1°$. The repose angle of the sand grains was determined as the embankment angle of a granular pile resulting from slowly pouring sand grains from a small height onto a horizontal surface. A seeding mixture of 1 part black particles to 4 parts light particles was found to give the best contrast results for the digital image analysis described below. The initial aspect ratio a, defined by the ratio of initial height, h_i, to initial basal length, d_i, was varied systematically over roughly two orders of magnitude. The initial basal lengths and range of aspect ratios for the different values of basal inclination are presented in table 1.

2.2. *Measurement methods*

After each experiment the maximum runout distance δd, the distance from the gate to the final front, was measured along the inclined plane (figure 1). Height profiles $h(x)$ of the final deposits were obtained by measuring the vertical height difference between the upper free surface and the inclined base at horizontal spacing of 2 cm.

Experiments were recorded by a fast camera at 120 frames $\mathrm{s^{-1}}$ to investigate the behaviour of the collapses through the vertical Plexiglas plane. From these movies we measured the instantaneous position of the flow front as a function of time, $d(t)$, and the time t_∞ when the motion of the flow front ceased.

Experiments with $a = 5$, 7 and 9 at inclinations of 4.2°, 15°, 20° and 25° were repeated to investigate the time-dependent form of the internal interface and velocity profiles with depth. With the fast digital camera at 120 frames $\mathrm{s^{-1}}$ (resolution 768×480), the entire flow was filmed through the transparent frontal pane. To obtain curves of the interface between static and flowing particles, $h_D(x, t)$, we first analysed every fifth and sixth frame using the Pattern Match algorithm of Dalziel (2005). Finally, we carefully corrected, as was necessary, these curves to match exactly the interface between the uppermost static and the lowermost flowing particle. Detailed velocity profiles with depth at a distance $\delta d/3$ from the gate were obtained by particle image velocimetry (PIV) analysis on digital high-speed camera footage using the

algorithm written by Dalziel (2005). The camera was operated at 1000 frames s^{-1} and a resolution of 640×512 pixels (24 bits). The focal plane with a horizontal length of 30 cm was illuminated by up to eight halogen spotlights to allow for shutter speeds of 1/2000 s and below. With these settings the 1.4 mm diameter particles were resolved at approximately 3 pixels in the mean flow direction. The interrogation area for the PIV was set to a square of 19 pixel length ($\sim$8.9 mm) and larger to capture maximum displacements in the flow of up to 2 mm between adjacent frames. The particle number of the 4:1 mixture of light grey to black particles in the interrogation area was always larger than 40.

3. Experimental observations

Much of the flow behaviour of granular collapse flows into rough, inclined channels is similar to that previously reported for collapses into horizontal channels (Huppert *et al.* 2003; Balmforth & Kerswell 2005; Lajeunesse *et al.* 2005; Lube *et al.* 2005; Lube *et al.* 2007). We will thus give a brief description of these collapses and elucidate the major differences between the two cases.

Upon suddenly lifting the gate, an initial discontinuity develops within the granular column separating a lower static from an upper moving region. In cross-section it is observed as a straight line intersecting at a zero height at $x = d_i$. This initial line is inclined at approximately 60° to the horizontal, independent of a and θ. Lajeunesse *et al.* (2005) have reported that for spherical glass beads (and $\theta = 0°$), this inclination is slightly lower but also independent of a. This discontinuity represents the initial shape of the internal interface, which propagates upwards as the grains run out and when it reaches the upper free surface the motion terminates.

Flow behaviour differs depending on whether or not the interface between static and moving grains intersects the surface of the column at the onset of motion. For aspect ratios $a < 1.7$ and for all tested basal inclinations, only an outer marginal part of the column is involved in the motion. As material flows downwards, the interface eventually reaches the upper free surface along the entire flow length. As for the horizontal case, there is a final stage of thin avalanching across the upper free surface before the motion stops entirely. For $a < 1$, some part of the initial upper surface of the column remains undisturbed (i.e. final height $h_\infty = h_i$), and the final deposit takes the form of a truncated wedge. For $1 < a < 1.7$, the entire upper free surface becomes mobilized in the late stage of the experiment resulting in a wedge-shaped deposit.

For larger aspect ratios $a > 1.7$, the entire upper free surface flows from the beginning. While there is continuous collapse for $1.7 < a < 2.8$, we observe two stages of motion for $a > 2.8$. Collapse begins with a free-fall phase, during which the upper part of the column above a critical height of approximately 2.8 d_i is in purely vertical motion (figures 2*a* and 3*a*). Once the upper free surface of the column has fallen to the critical height of 2.8 d_i, particles in the entire flowing region spread outwards (figures 2*b*, 2*c*, 3*b*, 3*c*). This second stage of motion is referred to as the lateral spreading phase.

This flow behaviour occurs up to basal inclinations of 20°, and the most noticeable effect of increasing θ is that the flows (at similar values of a and d_i) become progressively faster and thinner. For $\theta \leqslant 20°$, the internal interface reaches the free upper surface at almost the same time over the entire flow length and terminates the motion (figure 2*d*). However, at inclinations of 25° and for $a > 2.8$ the flow behaviour changes. Here the internal interface reaches the upper free surface of the rear region

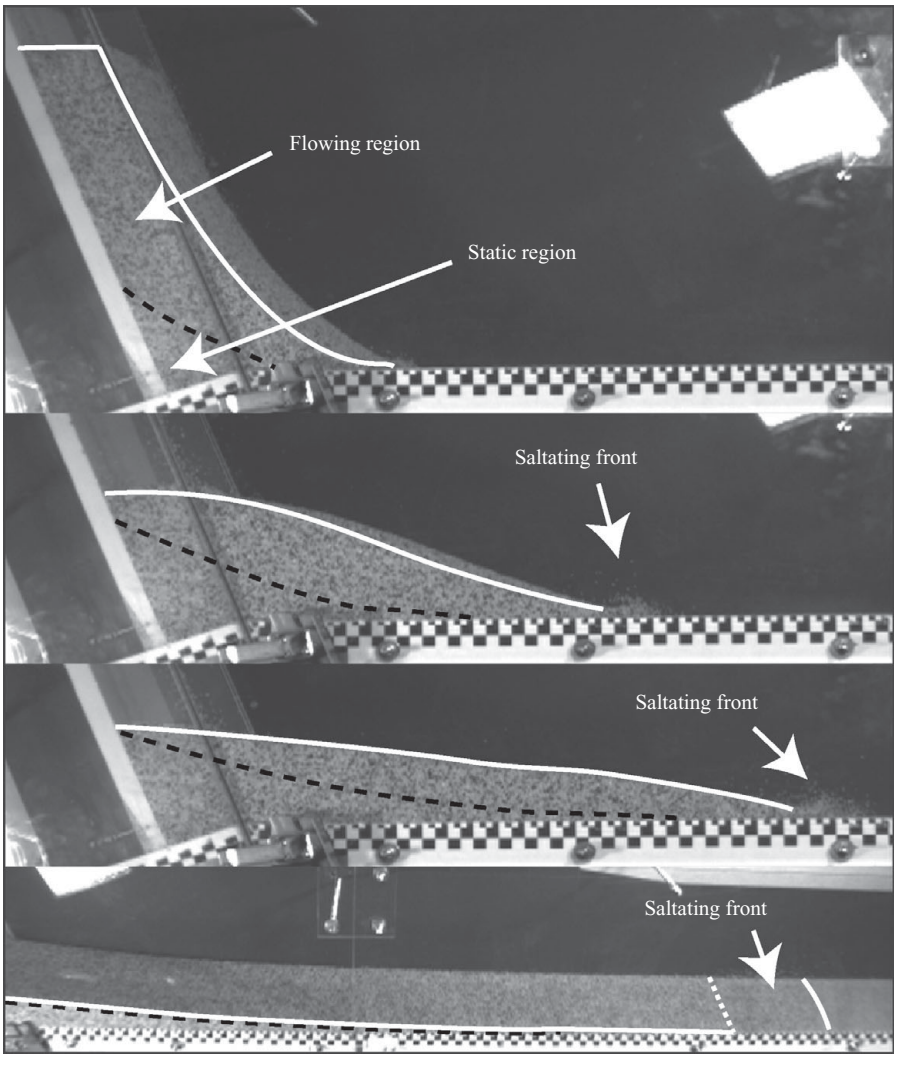

FIGURE 2. Flow evolution at different times, as marked in the top-left corner, for an experiment with $a = 7$, $d_i = 6.05$ cm and $\theta = 20°$. The internal interface between static and flowing regions (black, dashed curve), the upper free surface (solid, white curve) and the saltating front are highlighted.

first (and stops), while the frontal region propagates further as a mobile flow that thins out to a thickness of a few grain diameters (figure 3*d*).

In all experiments a frontal region of saltating grains precedes the coherent front (figures 2 and 3). The length of the saltating region increases with time and also with the basal inclination.

4. Final geometry

4.1. *Final height profiles*

The contours of the final deposits vary with both the initial aspect ratio and the basal inclination. To allow a comparison between all the profiles, here we consider

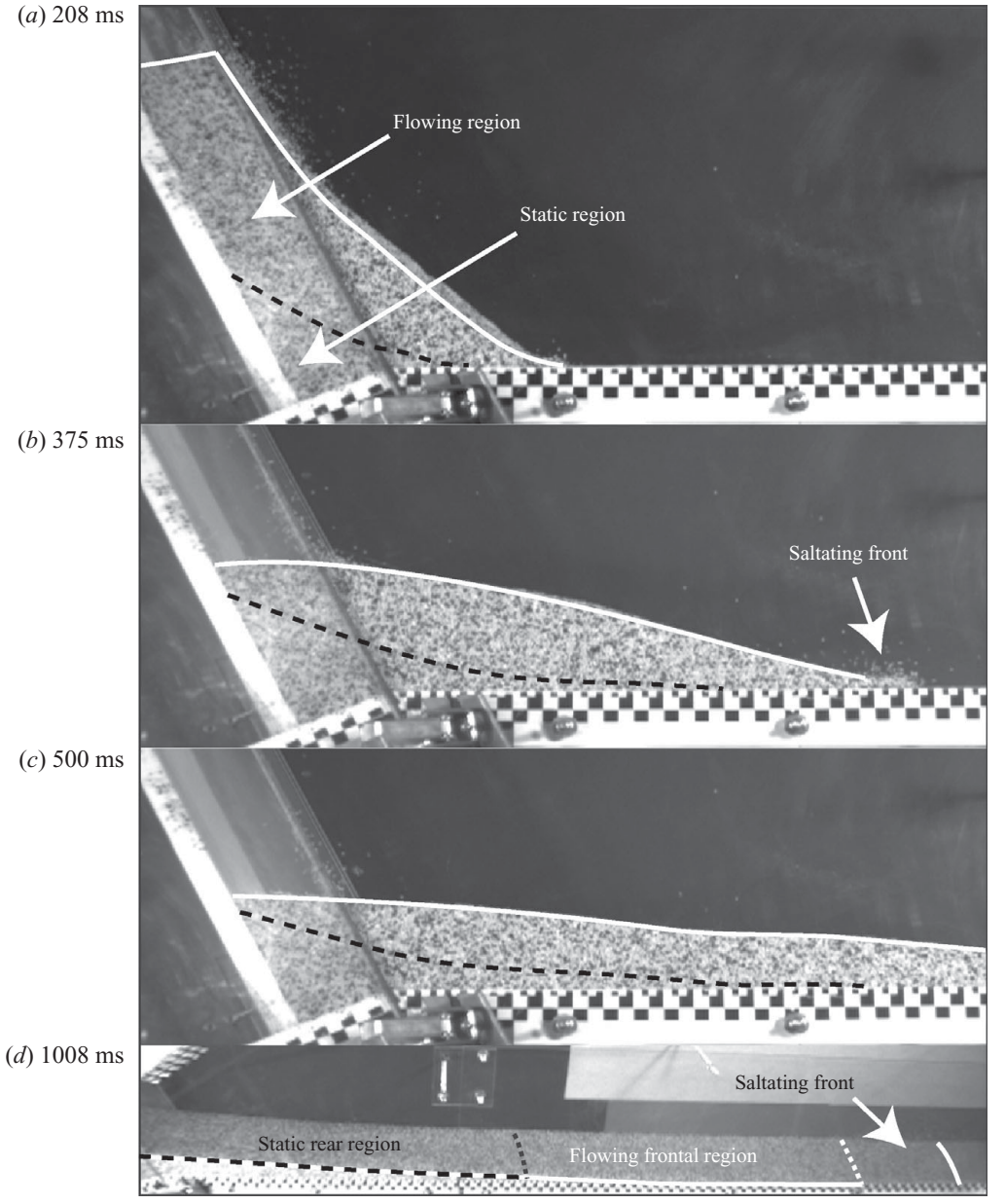

FIGURE 3. Flow evolution at different times for an experiment with $a = 7$, $d_i = 6.05\,\text{cm}$ and $\theta = 25°$. The internal interface between static and flowing regions (black, dashed curve), the upper free surface (solid, white curve) and the saltating front are highlighted. The interface reaches the free surface in the rear region first, while the frontal region is still propagating as a very shallow flow.

the vertical depth, $h(x)$, between the upper free surface and the inclined bottom plane sampled at regular horizontal spacing. In contrast to the inclined channel, the reservoir hosting the initial column of sand has a horizontal base. In experiments it does not make a difference whether the base of the reservoir is horizontal or similarly inclined as the channel. This is because the outer inclination of the initial interface

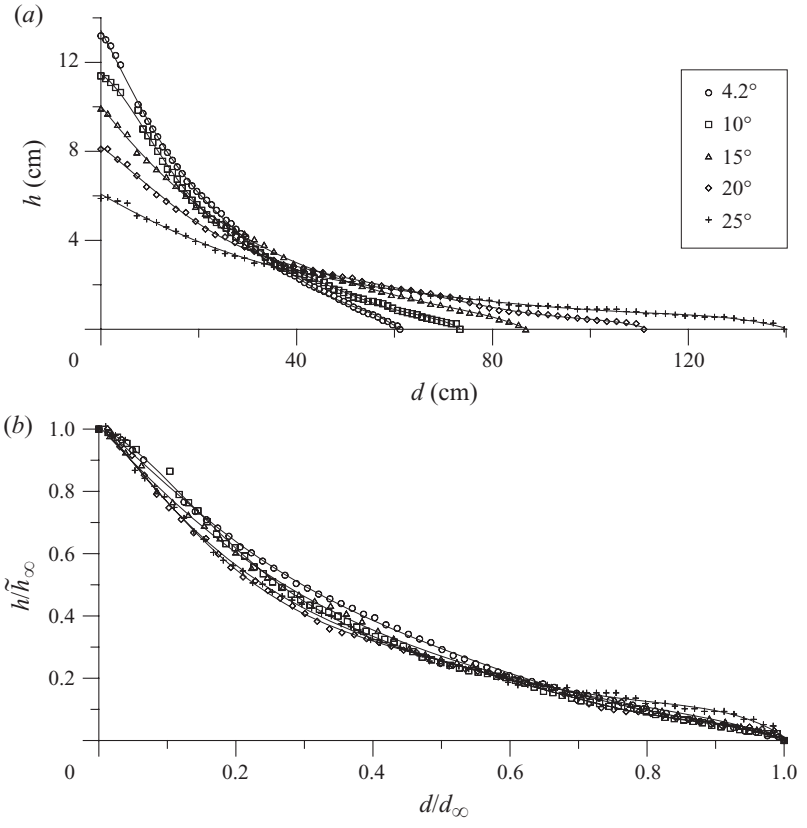

FIGURE 4. (*a*) Shape of final deposits for five experiments with constant initial height h_i ($\sim$ 44 cm) and basal length d_i (6.05 cm) at inclinations from 4.2° to 25°. (*b*) Shape of final deposits for the data in a non-dimensional form.

(ca. 60°) is always much larger than the channel inclination. Hence, and to allow for a simpler analysis of the final height profiles, the measured final deposit depths in the reservoir were reduced by $(d_i–x)\tan\theta$, as if the incline would reach into the reservoir. The influence of the basal inclination is illustrated in figure 4(*a*). This graph, which shows profiles of five experiments for constant $a = 7$ and θ varied from 4.2° to 25°, gives an impression how the deposits become progressively thinner and elongated with increasing inclination. The final profiles for experiments with varying aspect ratio, while θ is kept constant, are shown in figure 5(*a–e*). At inclinations of 4.2°, 10° and 25°, the profiles are relatively smooth curves with a steep rear segment and a flat outer segment. However, for experiments with $a > 7$ at $\theta = 15°$ and $\theta = 20°$, the profiles comprise a pronounced step-like disturbance in between these two segments whose amplitude and distance from the origin increase with the aspect ratio. The step-like disturbance forms when a surge-like wave, propagating from the upper surface of the collapsing column towards the flow front, separates a high-velocity frontal region from a lower velocity rear region.

The contours of the final deposits can be written in a non-dimensional form as

$$h(x)/\tilde{h}_\infty = \eta(x/d_\infty, a, \theta), \tag{4.1}$$

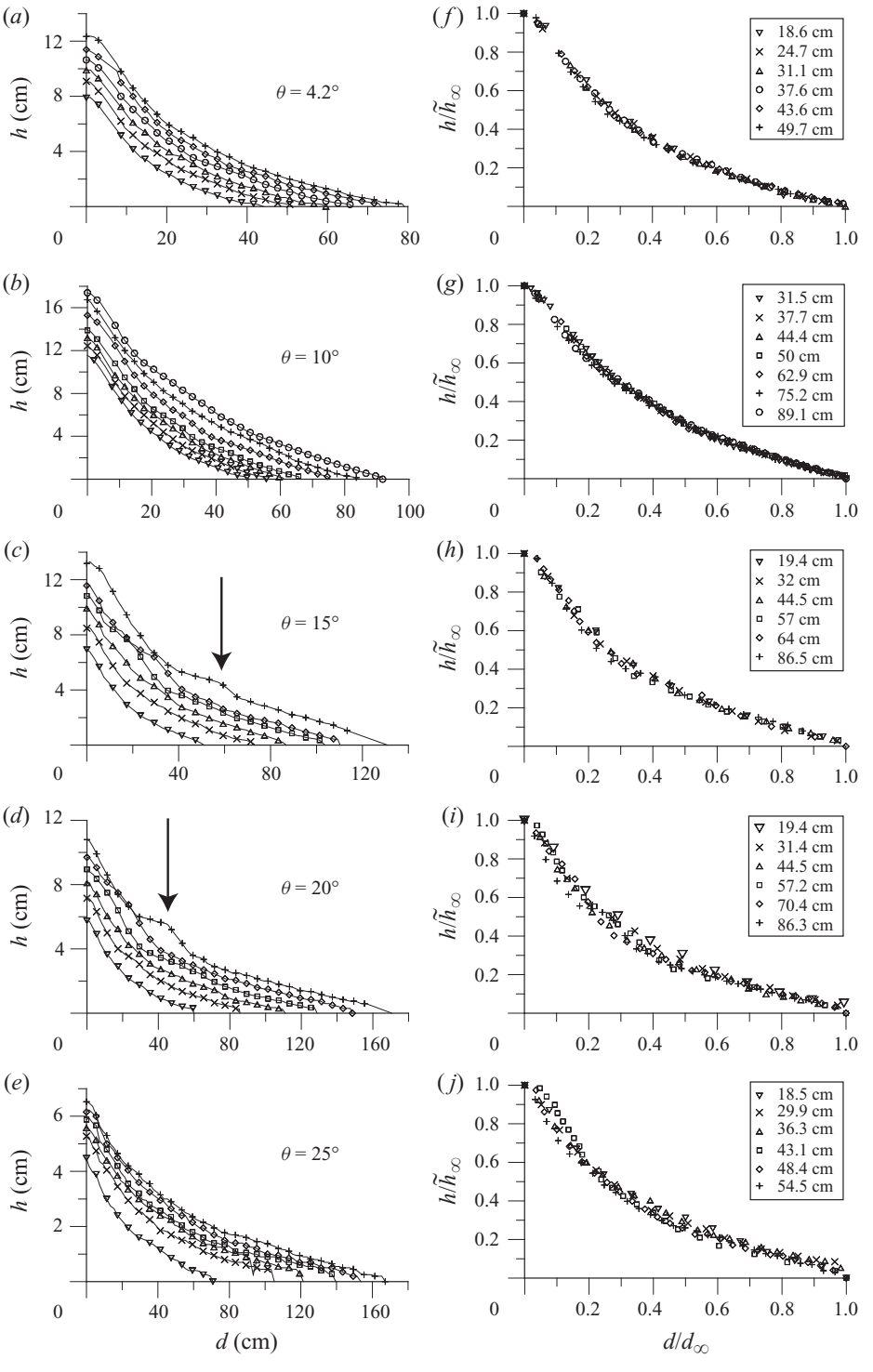

FIGURE 5. Non-normalized and normalized forms of the shape of final deposits for experiments with aspect ratios ranging from 3 to 14.3 for: (*a*, *f*) 4.2°, (*b*, *g*) 10°, (*c*, *h*) 15°, (*d*, *i*) 20° and (*e*, *j*) 25°. The arrows mark examples of the bump-like disturbance described in the text.

where $\tilde{h}_\infty = h_\infty - d_i \tan\theta$ and $d_\infty = \delta d + d_i/\cos\theta$. Lube *et al.* (2005) showed that for $\theta = 0^\circ$ in the second flow regime ($a > 2.8$), the height profiles obey a self-similar form of

$$h(x)/\tilde{h}_\infty = \tilde{\eta}(x/d_\infty, a), \tag{4.2}$$

where the non-dimensional profiles are independent of the aspect ratio. We will now test whether the function η can be split into two dimensionless functions $\tilde{\eta}$ and F_P as $h(x)/\tilde{h}_\infty = \tilde{\eta}(x/d_\infty, a)F_P(\theta)$ to allow a separate analysis of the effect of the aspect ratio and the basal inclination. For the function $\tilde{\eta}$ of x/d_∞ and a we know by definition that

$$\tilde{\eta}(0, a) = 1 \quad \text{and} \quad \tilde{\eta}(1, a) = 0. \tag{4.3}$$

In figure 5(*f–j*) the height profiles are presented in a non-dimensional form for each inclination. It is seen that there is a very good data collapse for $\theta = 4.2^\circ$ and $\theta = 10^\circ$ (as there is for $\theta = 0^\circ$, Lube *et al.* 2005). There is some minor scatter for the non-dimensional, collapsed profiles at $\theta = 15^\circ$ and $\theta = 20^\circ$, which, however, can be attributed to the step-like disturbances mentioned previously. In contrast to experiments with inclinations smaller or equal to 20°, non-dimensional height profiles for experiments at 25° do not collapse to one universal profile. Plotting the height profile data of figure 4(*a*) for $a = 7$ in a non-dimensional form (figure 4*b*) shows that there is a dependence on the basal inclination. To understand the function F_P better, we now analyse the dependence of d_∞ and h_∞ on a and θ.

4.2. *Scaling arguments for the maximum runout distance*

Experimental observations that the form of collapse differs with both the aspect ratio and the basal inclination immediately suggest using a and θ as the fundamental parameters for the analysis of the maximum runout distance. For $\theta = 0^\circ$, it was shown that a is the only parameter and, because inertial effects dominate frictional effects, the collapses are insensitive to changes of the particle characteristics (Huppert *et al.* 2003; Lajeunesse *et al.* 2004, 2005; Lube *et al.* 2004, 2005). Also, because most of the flow propagates on a layer of already deposited material, the flow behaviour is independent of basal friction δ_B (Lajeunesse *et al.* 2005; Lube *et al.* 2005, 2007). However, the resistance between static and moving particles, which has to be related to the internal friction angle ϕ, may be an important parameter to this problem. We thus assume that the maximum runout distance can be expressed by dimensional arguments as a function only of two separate non-dimensional terms for a and θ, ϕ:

$$\delta d = d_i \zeta(a) F_D(\theta, \phi). \tag{4.4}$$

For small values of a, where only the outer margin of the column takes part in the flow, the collapse is independent of d_i and (4.4) simplifies to

$$\delta d = k_L(\theta, \phi) h_i, \tag{4.5}$$

where k_L is dependent on the basal inclination and for $\theta = 0^\circ$, $k_L = 1.58$ for different grain forms and sizes (Lube *et al.* 2005). At a large aspect ratio, ζ depends on both h_i and d_i. For the case of $\theta = 0^\circ$, it was shown experimentally that $\zeta \propto a^{2/3}$ (Lajeunesse *et al.* 2005; Lube *et al.* 2005).

In figure 6(*a*) we plot the data of the maximum runout distance normalized by d_i for the different values of a and θ. For all values of θ and $a < 2.8$, δd varies linearly according to (4.5). At $a > 2.8$ and for $\theta \leqslant 20^\circ$, the data are well represented by power laws of the form

$$\delta d/d_i = k_H(\theta, \phi) a^{2/3} \tag{4.6}$$

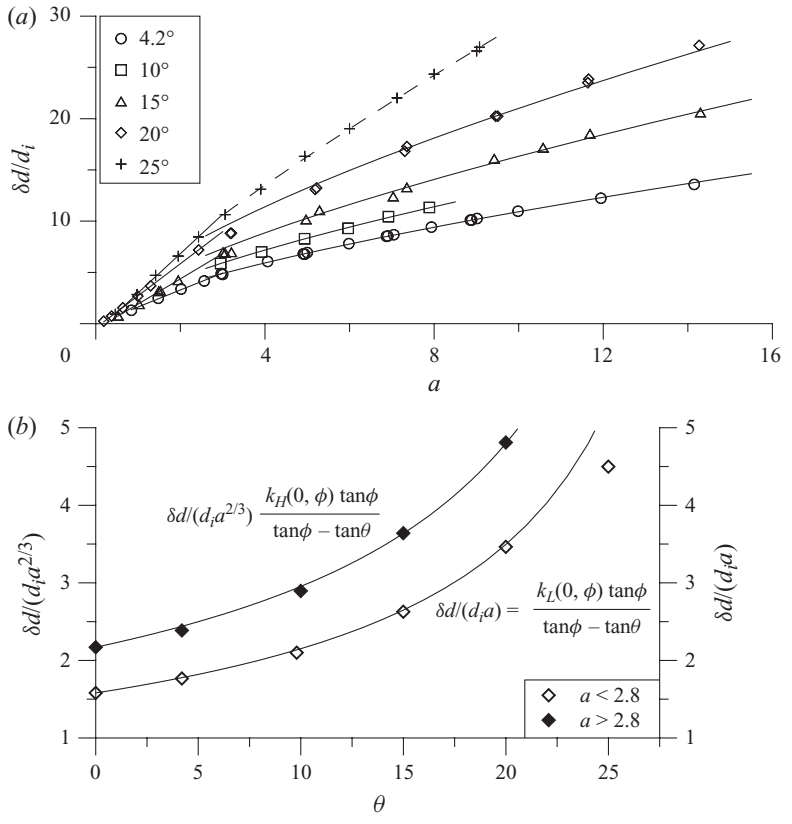

FIGURE 6. (*a*) The normalized maximum runout distance as a function of the aspect ratio for basal inclination ranging between 4.2° and 25°. Linear best fits are drawn to the data with $a < 2.8$. The solid curves for the experiments with $a > 2.8$ represent power law functions of the form $\delta d/d_i = k_H(\theta, \phi)a^{2/3}$. The dashed curve for the experiments at 25° represents the best-fit power law through the data for $a > 2.8$. (*b*) The analytical solutions (4.13) and (4.14) compared with the experimentally determined values for $k_H = \delta d/(d_i a^{2/3})$ for $a > 2.8$ and $k_L = \delta d/(d_i a)$ for $a < 2.8$ as a function of the basal inclination. Values of the internal friction angle determined by best fits of (4.13) and (4.14) to the data are almost identical (33.6° for the large-aspect-ratio regime and 33.8° for the low-aspect-ratio regime) and in agreement with the experimentally determined friction angle for the sand ($33 \pm 1°$).

and $k_H = 2.17$ for $\theta = 0°$ for different grain forms and sizes (Lube *et al.* 2005). For $\theta = 25°$ the runout data are not well described by a two-thirds power law. A best fit through the data gives $\delta d/d_i = 4.6a^{0.84}$. This deviation demonstrates the different flow behaviour that occurs when the basal inclination comes close to the AOR.

The above results can be usefully combined with the analytical solutions for granular dam-break flows by Mangeney, Heinrich & Roche (2000) to specify the functional form of F_D. The analytical solution for the position of the flow front d as a function of time is given by

$$d = 2c_0 t - \tfrac{1}{2}mt^2, \tag{4.7}$$

where, for the inclined flow problem, the terms c_0 and m are given by

$$c_0 = (kgh_i \cos\theta)^{1/2} \tag{4.8}$$

and

$$m = g\cos\theta(\tan\phi - \tan\theta), \tag{4.9}$$

with k being an empirical function of granular friction. Note that the basal friction angle in (4.8) and (4.9) has been replaced by the internal friction angle because the flows under consideration propagate on a layer of deposited particles and not over the rigid base of the chute. Equation (4.7) predicts that the flow stops at a time t_∞ given by

$$t_\infty = \frac{2c_0}{m} = \frac{2\,(kh_i/g\cos\theta)^{1/2}}{\tan\phi - \tan\theta}. \tag{4.10a, b}$$

Substituting (4.8), (4.9) and (4.10) into (4.7), we obtain

$$d(t_\infty) \equiv \delta d = \frac{2kh_i}{\tan\phi - \tan\theta} = \frac{2kad_i}{\tan\phi - \tan\theta}. \tag{4.11}$$

For the case $\theta = 0°$, (4.11) simplifies to

$$\delta d = \frac{2kad_i}{\tan\phi}, \tag{4.12}$$

while independent solutions for the final runout at $\theta = 0°$ are known through (4.5) and (4.6). This allows for substitution of the unknown function k to reveal a solution for the final runout distance for low and high aspect ratios as

$$\frac{\delta d}{d_i} = \frac{k_H(0,\phi)a^{2/3}\tan\phi}{\tan\phi - \tan\theta} \quad \text{(for large aspect ratios)} \tag{4.13}$$

$$\frac{\delta d}{d_i} = \frac{k_L(0,\phi)a\tan\phi}{\tan\phi - \tan\theta} \quad \text{(for small aspect ratios).} \tag{4.14}$$

A test of these relationships is shown in a graph of $\delta d/(d_i a)$ (for small aspect ratios) and $\delta d/(d_i a^{2/3})$ (for large aspect ratios) against θ (figure 6*b*). The agreement between theory and data is extremely good. Furthermore, numerical values of the internal friction angle determined through best fits of (4.13) and (4.14) to the data are almost identical for the low-aspect-ratio regime ($\phi = 33.8°$) and the high-aspect-ratio regime ($\phi = 33.6°$), and, importantly, they agree with the friction angle determined separately for the sand material used.

4.3. *Scaling arguments for the maximum height*

The maximum deposit height at $x = 0$ also depends on a and θ, and we assume that the mathematical description can be expressed as a function of two separate functions for a and θ, ϕ as

$$h_\infty = d_i\varphi(a)F_H(\theta,\phi), \tag{4.15}$$

where φ and F_H are dimensionless functions. These functions can be determined for small values of a, where $h_\infty = h_i$, and thus $\varphi(a) = a$ and $F_H = 1$, as demonstrated for the data $a \leqslant 1$ (figure 7*a*) For $a > 1$, best fits of the data for h_∞/d_i as a function of the aspect ratio indicate a power law of the form ma^n, where both m and n vary with θ. However, when instead of h_∞ the modified final height $\tilde{h}_\infty = h_\infty - d_i\tan\theta$ is plotted as $\tilde{h}_\infty/d_i$ against a (figure 7*a*), the data for $\theta \leqslant 20°$ are nicely represented in the form

$$\tilde{h}_\infty/d_i = c_H(\theta,\phi)a^{2/5}, \tag{4.16}$$

where, for $\theta = 0°$, $c_H = 1$ for different grain forms and sizes (Lube *et al.* 2005). As for the maximum runout distance, the final height data for $\theta = 25°$ at $a > 1$ cannot be

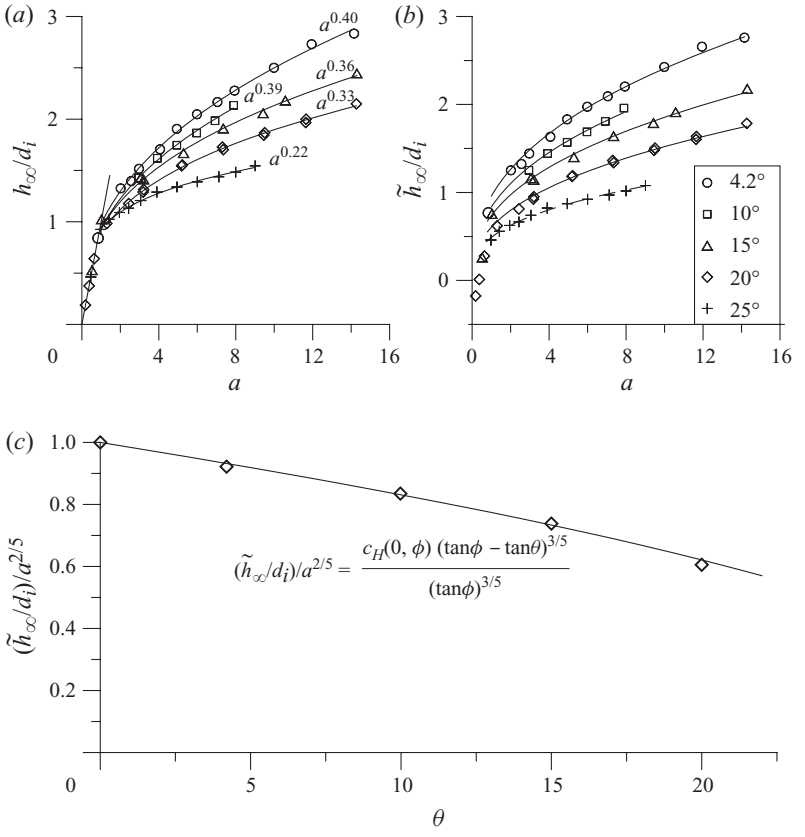

FIGURE 7. (*a*) The normalized maximum deposit height plotted as a function of the aspect ratio. (*b*) The modified maximum deposit height plotted as a function of the aspect ratio. The solid curves represent functions of the form $\tilde{h}_\infty/d_i = c_H(\theta,\phi)a^{2/5}$. The dashed curve shows the best-fit power law through the data for $\theta = 25°$. (*c*) Solution (4.18) compared with the experimentally determined values for $c_H(\theta,\phi) = \tilde{h}_\infty/(d_i a^{2/5})$ as a function of the basal inclination. The internal friction angle determined by best fit of (4.18) to the data equals 33.6°.

described by the same function as all the other data due to deviating flow behaviour. A best-fit power law through the data reveals $\tilde{h}_\infty/d_i = 0.49a^{0.36}$.

The good fit of solution (4.13) to the final runout data suggests that collapses on inclines are governed by three main parameters: the aspect ratio; a friction angle; which turns out to be the AOR; and the difference between the friction angle and the slope of the chute. This should be true for the final maximum height as well; only that runout and height are inversely related by some unknown function and we may write

$$\frac{\tilde{h}_\infty}{d_i} \propto \frac{a^{2/5} F_1(\tan\phi - \tan\theta)}{F_2(\tan\phi)}. \tag{4.17}$$

The variation of c_H with the basal inclination is presented in figure 7(*c*) showing the ratio $\tilde{h}_\infty/(d_i a^{2/5})$ plotted against θ. The data are well represented by the relationship

$$\frac{\tilde{h}_\infty}{d_i} = \frac{c_H(0,\phi)a^{2/5}\,(\tan\phi - \tan\theta)^{3/5}}{(\tan\phi)^{3/5}}, \tag{4.18}$$

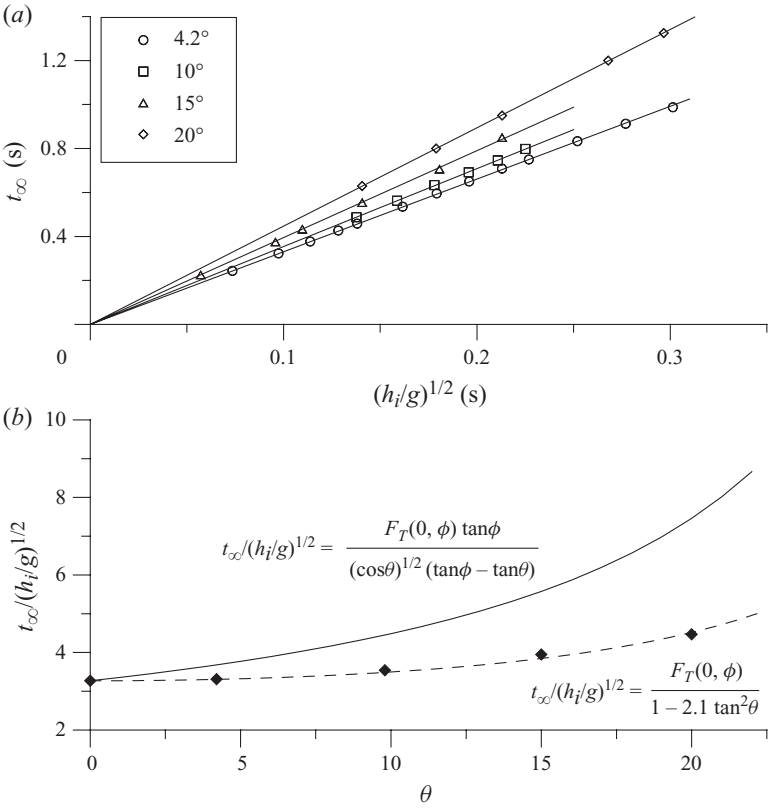

FIGURE 8. (*a*) The final time t_∞ plotted against the time scale $(h_i/g)^{1/2}$ for experiments with different aspect ratios and basal inclinations. (*b*) The experimentally determined values for $F_T(\theta,\phi) = t_\infty/(h_i/g)^{1/2}$ against the basal inclination. The solid line corresponds to the analytical solution (5.2), while the dashed line is a semi-empirical fit.

where $c_H(0,\phi) = 1$, and where F_1 and F_2 take power law forms with exponents of 3/5.

5. Flow front kinematics

The time, t_∞, at which the motion of the flow front ceases is determined from the temporal variation of the instantaneous flow front position. For $\theta = 0°$ this time depends only on the initial height h_i and g as $t_\infty \propto (h_i/g)^{1/2}$ (Lajeunesse *et al.* 2005; Lube *et al.* 2005). In analogy to the above arguments for the maximum runout and maximum height, we express t_∞ as

$$t_\infty = (h_i/g)^{1/2} F_T(\theta,\phi), \tag{5.1}$$

and figure 8(*a*) shows that the functional form of F_T is linear.

The variation of F_T with the basal inclination is shown in figure 8(*b*). An empirical fit of the data is given by the power law function $t_\infty/(h_i/g)^{1/2} = F_T(0,\phi) f(\theta)$, where $F_T(0,\phi) = 3.3$ for different grain forms and sizes (Lube *et al.* 2005) and $f(\theta) = 1/(1 - 2.1\tan^2\theta)$. The scatter of the data for $\theta = 25°$ is slightly too large for confident analysis.

Following the same approach as in § 4.2, we can use the analytical solution for t_∞ (10) from Mangeney, Heinrich & Roche (2000) and the scaling of F_T at $\theta = 0^\circ$ to derive the functional form of F_T and an analytical relationship for the final emplacement time as

$$\frac{t_\infty}{(h_i/g)^{1/2}} = \frac{F_T(0, \phi)\tan\phi}{(\cos\theta)^{1/2}(\tan\phi - \tan\theta)}. \tag{5.2}$$

Figure 8(*b*) reveals that this solution is a poor representation of the experimental data and it overestimates the runout times by as much as approximately a factor of 2. This sheds some light on the limitations of depth-averaged continuum models when applied to real-world granular flow problems.

Figure 9 shows the position of the flow front as a function of time for several experiments where θ was kept constant and the aspect ratio was varied from 3 to 14.3. There is an initial acceleration phase followed by a phase of approximately constant velocity before the flow fronts decelerate and stop. The initial acceleration is uniform at $0.75g$ and independent of the value of initial column height and the basal inclination. Transition to the second, constant velocity phase occurs approximately at a time $t = [2(2.5d_i)/(0.75g)]^{1/2}$ after the initial motion, also independent of h_i and θ. During the constant velocity phase, the flow front propagation is independent of the value of h_i. The magnitude of the constant velocity, however, does increase with the basal inclination.

6. Static and moving regions

6.1. *Motion of the internal interface*

The deposition of particles below the moving internal interface between static and moving particles was analysed in two ways. First, the bulk deposit volume per unit width, represented by the area A_D, integrated under the entire internal interface, was determined as a function of time for different values of a and basal inclinations of 15°, 20° and 25°. Second, in order to characterize vertical deposition rates along the flow, we measured the thickness of the static region, $h_D(d, t)$, at fixed distances, d.

The typical form of curves A_D against time is shown in figure 10(*a*) for four experiments at 15° and aspect ratios varying from 5.3 to 14.3. The data are plotted as A_D–A_W against time, where $A_W = 0.5d_i^2\tan 60^\circ$ is the area of the initial static wedge. The two phases of collapse, the initial free-fall phase and the subsequent lateral spreading phase, are evident in this graph. In the free-fall phase the static area increases with time independent of the initial height. The collapsed data follow the relationship A_D–$A_W \propto t^2$. At a time depending on a, the data depart from this universal curve and the static area increases at a lower rate. For the two large-aspect-ratio experiments with $a = 10.6$ and $a = 14.3$, A_D varies approximately linearly with time in this lateral spreading phase such that the deposition rate $\mathrm{d}A_D/\mathrm{d}t$ is effectively constant. For the two experiments with $a = 5.3$ and $a = 7.3$, however, the deposition rate in the lateral spreading phase is not constant but increases with time.

The principal effect of the basal inclination on the deposition behaviour is demonstrated in figure 10(*b*). Here the data A_D–A_W against time are shown for four experiments at 0°, 15°, 20° and 25°, where h_i ($\sim$ 44 cm) and d_i (6.05 cm) were kept constant. In the free-fall phase, the data overlap and the static area increases with time independent of the basal inclination. While the data overlap in the free-fall phase, there is a strong variation with the basal inclination in the lateral spreading phase such that the deposition rate strongly decreases with increasing θ at any given time.

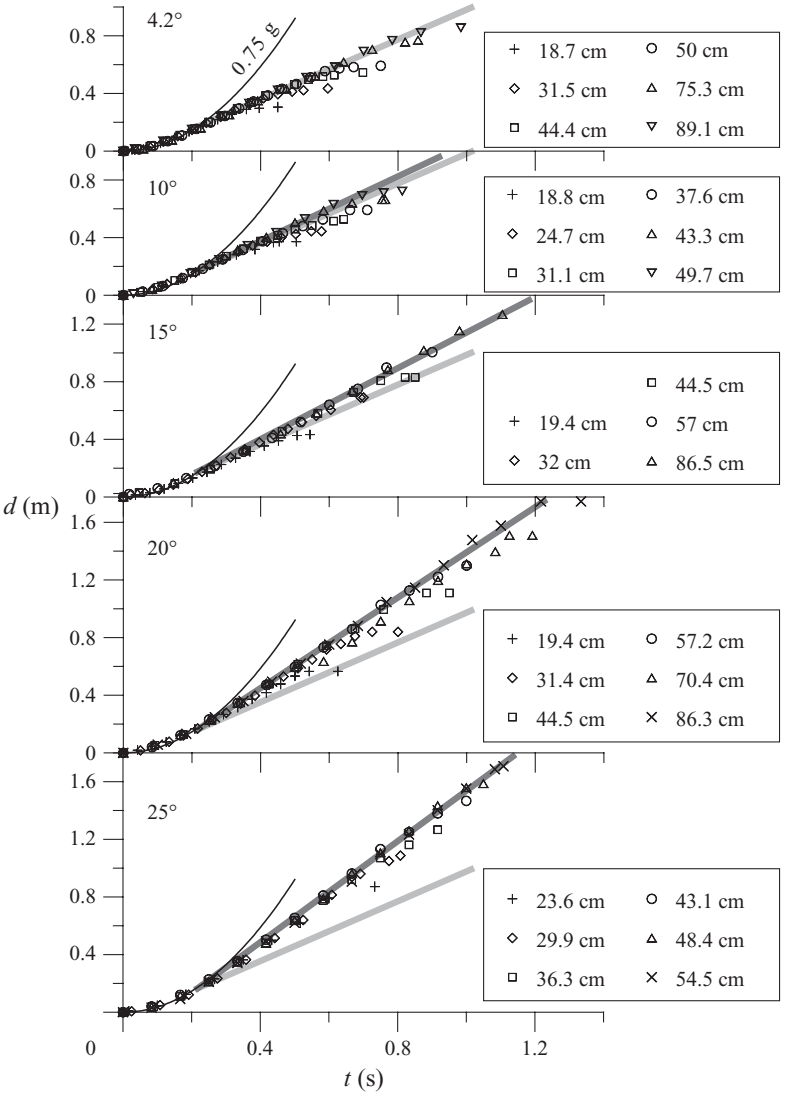

FIGURE 9. The position of the flow front as a function of time for 4.2°, 10°, 15°, 20° and 25°. Curves of $d = 0.5 \cdot 0.75 \cdot gt^2$ nicely describe the initial, uniform acceleration phase which is independent of h_i and θ. The dark grey line highlights the constant gradient during the lateral spreading phase. For comparison purposes, the gradient obtained for experiments at 4.2° is repeated in the other plots as the light grey line.

Unfortunately, due to poorer resolution of the high-speed footage with increasing flow length, the data at 20° and 25° are slightly too scattered to be further analysed with confidence.

Results for the second approach to analysing the thickness variation of the static region over time at fixed distances d are shown in figure 11(a), where h_D ($d = \text{const.}$) is plotted against time at regular spacing of 5 cm for an experiment with $a = 7.3$ and $\theta = 15°$. At proximal distances $d = 10$ cm, 15 cm and 20 cm, h_D initially increases with time in a nonlinear fashion followed by approximately linear segments. The initial part is observed during the free-fall phase, whereas the final linear segment occurs during

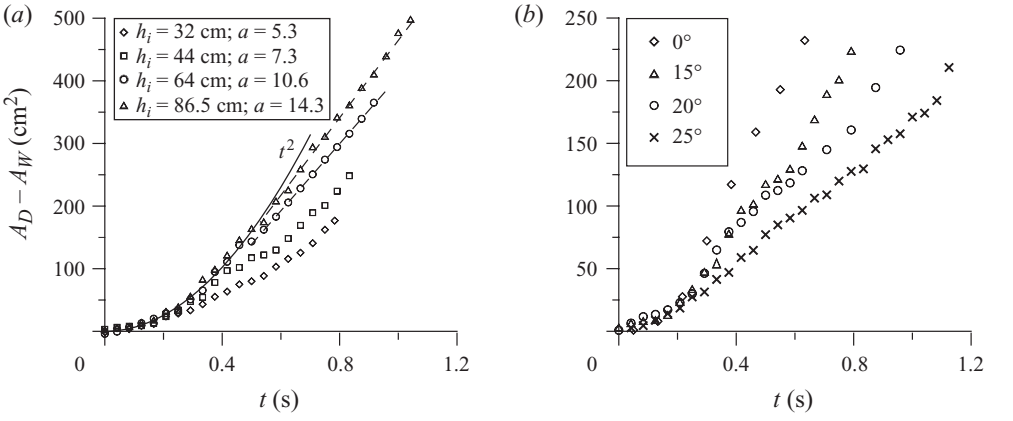

FIGURE 10. (*a*) The deposited area below the internal interface as a function of time for four experiments at 15°. (*b*) The deposited area as a function of time for three different basal inclinations and constant h_i (~ 44 cm) and d_i (6.05 cm).

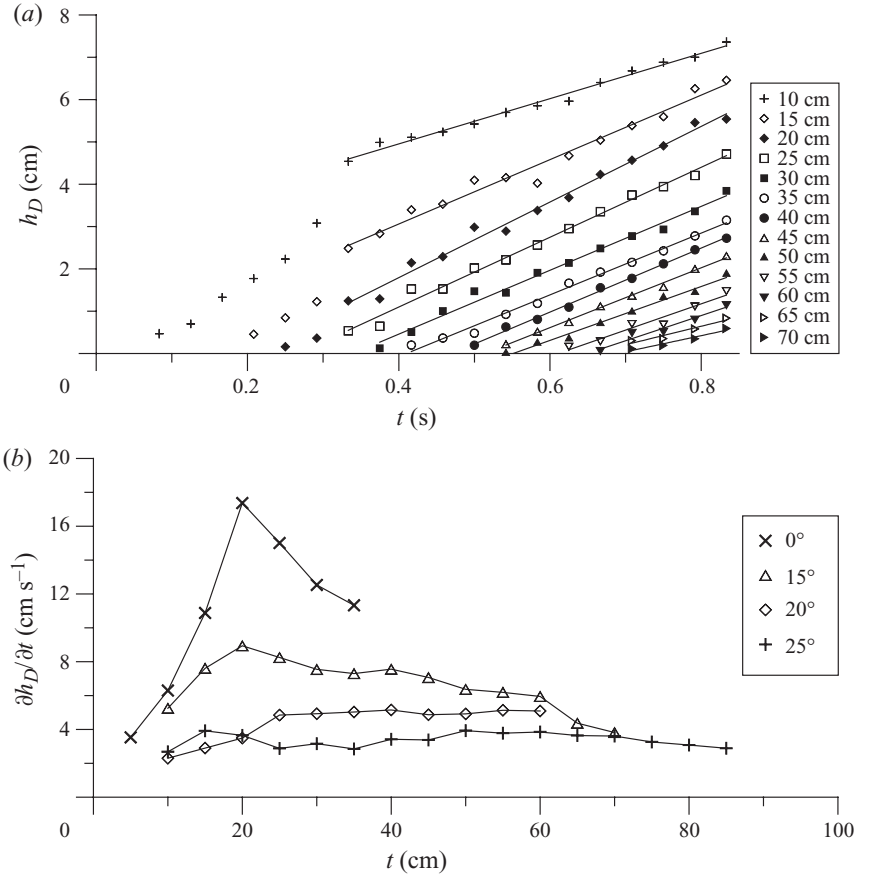

FIGURE 11. (*a*) Thickness variation of the static region as a function of time at fixed longitudinal spacing of 5 cm for an experiment at 15° basal inclination where $a = 7.3$ and $d_i = 6.05$ cm. The solid lines represent linear best fits through the data in the lateral spreading phase. (*b*) The local deposition rate $\partial h_D/\partial t$ against the longitudinal distance from the gate for experiments with different basal inclinations and constant h_i (~ 44 cm) and d_i (6.05 cm).

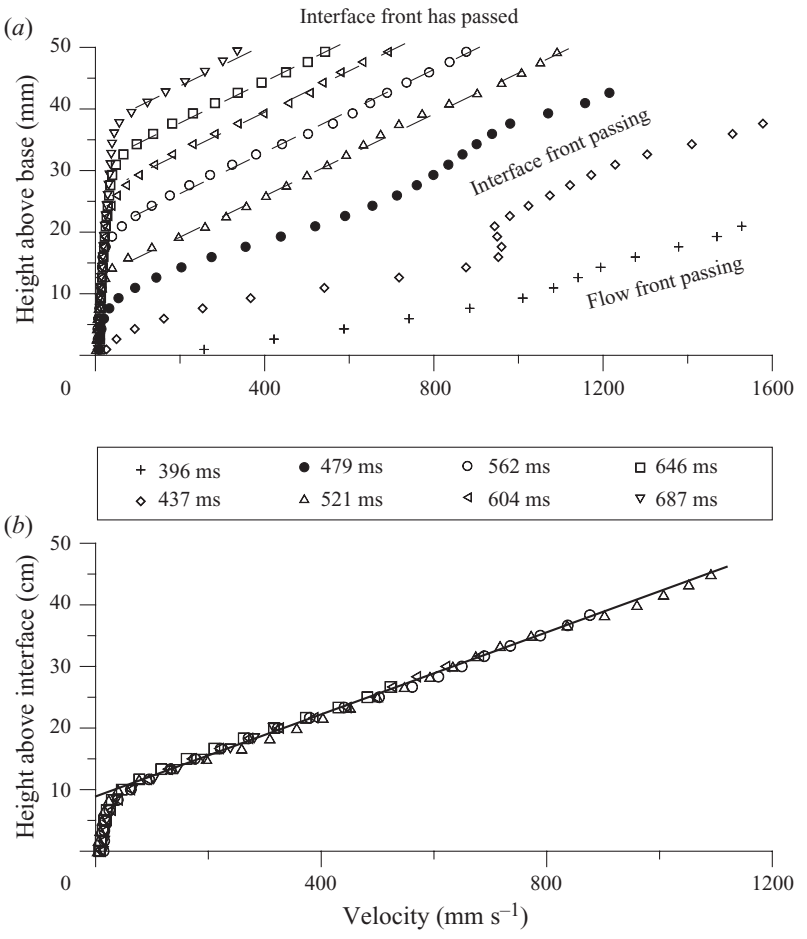

FIGURE 12. (*a*) Example of the velocity profiles perpendicular to the base at different times for an experiment at $\theta = 4.2^\circ$ and $a = 6.7$. (*b*) Collapse of the same velocity data (for $t \geqslant 521$ ms) plotted as velocity against height above the internal interface.

the lateral spreading phase. At distal positions ($d > 20$ cm), the temporal increase in h_D is entirely linear and governed by lateral spreading only. The linearity of the data during the lateral spreading phase allows the calculation of local deposition rates $\partial h_D/\partial t$ from linear best fits. In figure 11(*b*) the data $\partial h_D(d, t)/\partial t$ for inclinations of 15°, 20° and 25° at constant h_i and d_i are compared to the corresponding data for $\theta = 0^\circ$. The local deposition rate varies along the flow length. A proximal increase close to the gate is followed by slightly decreasing or approximately constant values. The local deposition rate strongly decreases with increasing inclinations, although there is some scatter in the data for high values of θ.

6.2. *Velocity profiles*

Velocity profiles in the flowing layer have been analysed normal to the inclined plane at the fixed position $\delta d/3$ from the gate. The flow front approaches this distance in the lateral spreading phase. Two different kinds of profile geometries are observed. The velocity profile is typically S-shaped with a high slip velocity at the base and lower shear rate close to the upper free surface (figure 12*a* at 396 ms) during

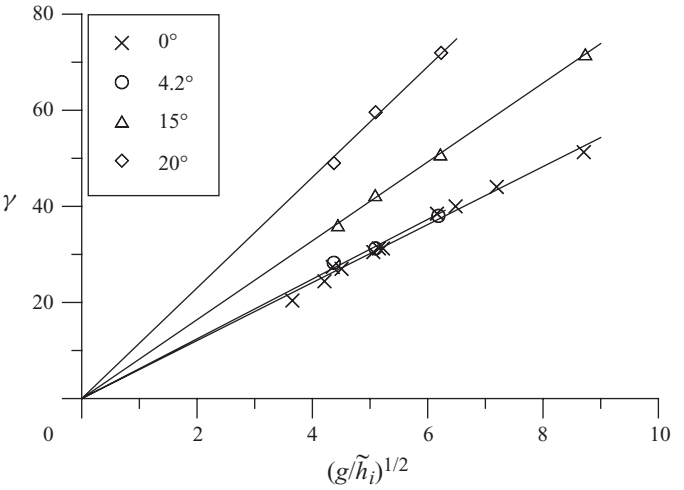

FIGURE 13. Experimentally determined shear rates against the shear rate scale $(g/\tilde{h}_i)^{1/2}$ for basal inclinations varying from 0° to 20°.

passage of the frontal region with direct contact to the base. With the arrival of the internal interface front at the observation point, the velocity profiles exhibit a complex transitional shape in which a central low-shear zone separates the lower and upper regions in which the shear rate increases with height (figure 12*a* at 437 and 479 ms). Shortly afterwards, when the interface front has passed, the velocity profiles change to a thin lower exponential region immediately above the interface followed by an upper linear region (figure 12*a* at 521–687 ms). This profile shape is maintained for the remaining duration of flow.

Subtraction of the thickness of static grains below the interface from the height values in figure 12(*a*) to obtain the height in the flowing layer reveals that the velocity profiles formed after passage of the interface front collapse to a universal profile (figure 12*b*) for each aspect ratio and at basal inclinations $\theta \leqslant 20°$. This data collapse, however, does not work for the experiments at 25°. At such steep inclination, the velocity profiles after passage of the interface front still comprise a lower exponential and an upper linear region, but the slope of the linear section varies with time.

A shear rate can be calculated as the inverse slope of the linear section of the collapsed universal profile. Lube *et al.* (2007) have shown that for $\theta = 0°$ this shear rate follows the relationship

$$\gamma_0 = 6.1(g/\tilde{h}_i)^{1/2}, \tag{6.1}$$

where $\tilde{h}_i$, defined by

$$\tilde{h}_i = h_i - d_i \tan(60°)/2, \tag{6.2}$$

is a length scale that describes the fraction of the granular column actually involved in the flowing region. We adopt this relationship for the data for inclined channels investigated here. In figure 13 we show the experimentally determined shear rates against the shear rate scale $(g/\tilde{h}_i)^{1/2}$ for the different inclinations. While the data for 0° and 15° include the full range of aspect ratios, only experiments for $a = 5$, 7 and 9 were analysed for the other inclinations. Anyhow, the data can be approximated by linear functions of the form $\gamma(\theta, \tilde{h}_i) = c_S(\theta)(g/\tilde{h}_i)^{1/2}$. The general tendency of increasing c_S with the basal inclination is evident.

7. Summary and conclusions

Experimental results for the collapse of rectangular columns of sand into rough, inclined channels are presented. Both the shape of final deposits and the kinematic behaviour were analysed as functions of the initial aspect ratio and the basal inclination of the channel.

The main results from the analysis of the resulting deposits are as follows.

(i) Two different flow regimes at low and large aspect ratios exist, exactly as for collapses into horizontal channels.

(ii) In the range of tested basal inclinations, the final deposits for $a > 2.8$ and $\theta \leqslant 20^\circ$ can be described by a self-similar form with respect to their maximum horizontal and longitudinal extent.

(iii) For $\theta \leqslant 20^\circ$, analytical solutions for the shallow-water dam-break problem (Mangeney, Heinrich & Roche 2000) can be usefully combined with scaling relationships of the final runout distance and the maximum deposit height at zero inclination. This reveals the functional forms for δd and h_∞ as multiplicative functions of separate terms for the aspect ratio, the internal friction angle and the difference between this friction angle and the basal inclination.

In addition, the analysis of the kinematic behaviour revealed the following results.

(i) While shallow-water theory proves useful for the prediction of the maximum horizontal and vertical extents of the deposits, it largely overestimates the overall time to reach the maximum runout distance. This limitation, probably arising from neglecting vertical acceleration during the initial stages of collapse and from integrating over any vertical structures in the depth-averaged scheme, should be considered carefully when applying shallow-water granular models to real-world problems such as avalanches of debris and snow or debris flows.

(ii) The change in flow behaviour from the free-fall phase to the lateral spreading phase also affects the deposition from the base of the internal interface. At constant θ, the deposition rate in the free-fall phase is independent of the initial height and a, and scales like $\mathrm{d}A_D/\mathrm{d}t \propto t$. The deposition rate during the lateral spreading phase, however, increases with the initial height and decreases with increasing basal inclination.

(iii) The shear rate measured in the lateral spreading phase at a fixed longitudinal distance $\delta d/3$ from the gate increases with the basal inclination. The shear rate can be expressed as $\gamma(\theta, \tilde{h}_i) = c_S(\theta)(g/\tilde{h}_i)^{1/2}$, where c_S is an increasing function of the basal inclination.

The above conclusions apply to channel inclinations of $\theta \leqslant 20^\circ$. For a steeper inclination of $\theta = 25^\circ$, the flow behaviour differs by the development of a separation into both vertical (as for $\theta \leqslant 20^\circ$) and longitudinal regions of static below and behind moving material. This results in a different shape of the final deposit, as indicated by the values of δd and h_∞, such that the final runout distance for $a > 2.8$ follows a power law of the form $\delta d/d_i = 4.6a^{0.84}$ instead of $\delta d/d_i \propto a^{2/3}$ which is the case for $\theta \leqslant 20^\circ$. Assuming that all potential energy of the initial columns is dissipated by frictional forces (e.g. $\mu M_i g \delta d = M_i g h_i$, where M_i is the mass of the initial column), the maximum runout distance should follow the linear relationship $\delta d/d_i \propto a$. This suggests that the increase of the power law exponent to higher basal inclinations, probably approaching the value of 1, can be interpreted as a transition from inertial to more frictionally determined flow. At $\theta = 25^\circ$, the frontal region decouples from the main flow and travels further as a thin sheet flow only a few particle diameters thick which is more strongly governed by frictional effects. Further experiments are

needed to show how this flow region responds to variations of the basal roughness and granular materials with different static angles of repose.

It will be interesting to explore in the future how the kinematical behaviour changes when the basal inclination approaches and exceeds the static AOR. An immediate assumption from our experimental findings is that for flows at the AOR, where a flow regime of steady, uniform motion develops, the internal interface coincides with the rigid base. Experiments on granular collapse flows down inclined channels at or above the AOR over a bed of loose particles might show that the interface propagates downwards, effectively causing erosion.

For the construction of the experimental set-up and data acquisition the help from Sebastian Muenn, Stefan Schulze, Carla Wiegers and Carlos Cabezas Banda was invaluable. We would like to thank Anne Mangeney for helpful discussions about analytical solutions for granular dam-break problems and three anonymous reviewers who helped clarifying the ideas presented. This study was supported by the Deutsche Forschungsgemeinschaft (grant Fr947/9-2) and the NZ-based Marsden Fund (09_MAU_110). G.L. is grateful for the support of a David-Crighton Fellowship awarded by the University of Cambridge and a Feodor-Lynen Postdoctoral Fellowship awarded by the Alexander-von-Humboldt Foundation. H.E.H. and R.S.J.S. acknowledge Royal Society Wolfson Research Merit awards.

REFERENCES

Balmforth, N. J. & Kerswell, R. R. 2005 Granular collapses in two dimensions. *J. Fluid Mech.* **538**, 399–428.

Dalziel, S. B. 2005 DigiFlow User Guide. Available at: http://www.damtp.cam.ac.uk/lab/digiflow/.

Doyle, E. E., Huppert, H. E., Lube, G., Mader, H. M. & Sparks, R. S. J. 2007 Static and flowing regions in granular column collapses down channels: insights from a sedimenting shallow water model. *Phys. Fluids* **19**, 106601, 1–16.

G.D.R. Midi 2004 On dense granular flows. *Eur. Phys. J.* E **14**, 341.

Gauer, P., Rammer, L, Kern, M., Lied, K., Kristensen, K. & Schreiber, H. 2006 On pulsed Doppler radar measurements of avalanches and their implication to avalanche dynamics. *Geophys. Res. Abstracts* **8**, 04683.

Huppert, H. E., Hallworth, M. A., Lube, G. & Sparks, R. S. J. 2003 Granular column collapses. *Bull. Am. Phys. Soc.* **48**, 68.

Huppert, H. E., Lube, G., Sparks, R. S. J. & Hallworth, M. A. 2004 In *Granular Column Collapse. ICTAM Proceedings.* Kluwer.

Hutter, K., Koch, T., Pluss, C. & Savage, S. B. 1995 The dynamics of avalanches of granular materials from initiation to runout. Part II. Experiments. *Acta Mech.* **109**, 127.

Kerswell, R. R. 2005 Dam break with Coulomb friction: a model for granular slumping? *Phys. Fluids* **17**, 057101, 1–16.

Lajeunesse, E., Mangeney-Castelnau, A. & Vilotte, J. P. 2004 Spreading of a granular mass on a horizontal plane. *Phys. Fluids* **16**, 2371–2381.

Lajeunesse, E., Monnier, J. B. & Homsy, G. M. 2005 Granular slumping on a horizontal surface. *Phys. Fluids* **17**, 103302.

Larrieu, E., Staron, L. & Hinch, E. J. 2006 Raining into shallow water as a description of the collapse of a column of grains. *J. Fluid Mech.* **554**, 259–270.

Lube, G., Huppert, H. E., Sparks, R. S. J. & Freundt, A. 2005 Collapses of two-dimensional granular columns. *Phys. Rev.* E **72**, 041301, 1–10.

Lube, G., Huppert, H. E., Sparks, R. S. J. & Freundt, A. 2007 Static and flowing regions in granular column collapses down channels. *Phys. Fluids* **19**, 043301, 1–9.

Lube, G., Huppert, H. E., Sparks, R. S. J & Hallworth, M. A. 2004 Axisymmetric collapses of granular columns. *J. Fluid Mech.* **508**, 175–199.

Mangeney, A., Heinrich, P. & Roche, R. 2000 Analytical solution for testing debris avalanche numerical models. *Pure Appl. Geophys.* **157**, 1081–1096.

Mangeney-Castelnau, A., Bouchut, B., Vilotte, J. P., Lajeunesse, E., Aubertin, A., & Pirulli, M. 2005 On the use of Saint–Venant equations for simulating the spreading of a granular mass. *J. Geophys. Res.* **110**, B09103, 1–17.

Pouliquen, O. 1999 Scaling laws in granular flows down rough inclined planes. *Phys. Fluids* **11**, 542.

Pouliquen, O. & Forterre, Y. 2002 Friction law for dense granular flows: application to the motion of a mass down a rough inclined plane. *J. Fluid Mech.* **453**, 131.

Savage, S.B. & Hutter, K. 1989 The motion of a finite mass of granular material down a rough incline. *J. Fluid Mech.* **199**, 177.

Siavoshi, S. & Kudrolli, A. 2005 Failure of a granular step. *Phys. Rev.* E **71**, 051302,1–6.

Staron, L. & Hinch, E. J. 2005 Study of the collapse of granular columns using 2D discrete grains simulation. *J. Fluid Mech.* **545**, 1–27.

Thompson, E. L. & Huppert, H. E. 2007 Granular column collapses: further experimental results. *J. Fluid Mech.* **575**, 177–186.

Zenit, R. 2005 Computer simulations of the collapse of a granular column. *Phys. Fluids* **17**, 031703, 1–4.